nature communications

Article

https://doi.org/10.1038/s41467-025-60720-6

Photo-controlled vacancies and conductivity within single crystals of silver chalcogenolate cluster-based MOFs

Received: 3 December 2024

Accepted: 29 May 2025

Published online: 01 July 2025

Check for updates

Kai Ma[1], Xue-Mei Liu[1], Xi-Yan Dong[1,2], Xi-Ming Luo[1], Hai-Yang Li[1] ✉, Shuang-Quan Zang[1] ✉ & Thomas C. W. Mak[1,3]

Structural vacancies in crystalline solids have great potential in tuning optoelectronic properties for specific applications. However, the random distribution of vacancies is still an intractable problem when creating materials with completely reproducible functions. Here, we report that the growth of crystals from solution approaching perfect single crystallization of assembled silver clusters (**SC-1**, where SC denotes single crystal), featuring a two-dimensional (2D)-three-dimensional (3D) interpenetrating conformation. By controlling the ultraviolet (UV) irradiation time, **SC-1** transformed into **SC-2-0.8** and then into **SC-2-0.5**, where partial trifluoroacetic acid (TFA) and the linker molecules (1,2,4,5-tetracyanobenzene, termed TCNB) possessed a 0.8 or 0.5 occupancy in the crystallography, forming ordered vacancies at specific sites. This course led to a deepened color, a diminished photoluminescence, a narrowed energy gap, and an average 50-fold increase in the single-crystal electron conductivity, together with a 3D-3D interpenetrating conformation. Over time, under the original conditions, **SC-1** regrew into **SC-3**, which had a 3D noninterpenetrating conformation with no crystallographic vacancies and a conductivity similar to that of **SC-1**. This work elucidates the correlation between the tunable vacancy number and electrical conductivity at the atomic level, providing a method for facilitating electronic communication between cluster-building units and creating ordered-vacancy conducting materials.

Crystalline solids are promising in modern optoelectronic technologies, ranging from solar cells and lithium-ion batteries to quantum computers, which require a specific conductivity[1]. Metal clusters are collections of metal atoms that are intermediate in size between a molecule and a nanoparticle or a quantum dot and constitute a structural model for the underlying function-oriented mechanism in nanoparticles and interparticle interactions within assembled materials[2–13]. The assembled metal clusters and metal chalcogenide clusters have conductivities in the range of semiconductors[14–16]. Yang et al. reported an increase in the conductivity of metal chalcogenide clusters, mixed with $Co_6Se_8(PEt_3)_6$ and $Cr_6Te_8(PEt_3)_6$ by fusing fullerenes in the matrix of the crystal lattice[17]. Li et al. used $[Cl]^-$ ions to assemble $[Au_{21}(SR)_{12}(PCP)_2]^+$ into a 1D structure with a conductivity of 2.38×10^{-8} S cm^{-1}, which is higher than the value obtained via $[AgCl_2]^-$ assembly of 1.44×10^{-10} S cm^{-1}[18]. Yuan et al. assembled $(AuAg)_{34n}$ clusters through Ag–Au–Ag bonds and achieved a maximum conductivity of 1.49×10^{-7} S cm^{-1} along the linkage direction[19]. Bootharaju et al. reported that $Cd_{14}Se_{13}$, protected by tetramethyl ethylenediamine and bridged by $[Cl]^-$ ions, exhibited semiconducting properties[20]. These assembled cluster crystals with extended structures have

[1]College of Chemistry, Zhengzhou University, Zhengzhou, China. [2]College of Chemistry and Chemical Engineering, Henan Polytechnic University, Jiaozuo, China. [3]Department of Chemistry, The Chinese University of Hong Kong, Shatin, New Territories, Hong Kong SAR, China.
✉e-mail: lihaiyang@zzu.edu.cn; zangsqzg@zzu.edu.cn

demonstrated potential in optoelectronic fields; however, developing a strategy and a method to facilitate electronic communication remains challenging[21–27].

Crystals exhibiting a periodic order that containing disorder or vacancies, can exhibit unique functionalities, termed disordered crystalline functional materials[28]. Disorder–order transitions of some specific compositions in crystals are related to the onset of the ferroelectricity within organic-inorganic perovskites[29]; Partial vacancy-type defects have been designed to tune the superconducting properties of $YBa_2Cu_3O_{6+x}$ crystals[30] or vary the mechanical, sorption and catalytic behavior of Prussian blue analogues[31,32] and metal-organic framework (MOF) crystals[33,34]. Therefore, embedding ordered vacancies in single crystals for targeted functionality has excellent potential. However, there are no reports of the modulation of the conductivity of assembled cluster crystals through the vacancy defect strategy. Metal clusters have sufficient flexibility for distortion and tolerance to diverse vacancy defects[35,36] owing to diverse metal–ligand ligation model and the cohesion effect arising from metal–metal interactions or bonds[37,38]. Anomalous unique electronic, magnetic, optical functionalities and mechanical properties could be brought out by some vacancies in cluster-assembled crystals, which would facilitate electronic communication in crystalline solids and support future applications in optoelectrical fields.

Here, we demonstrate vacancy-correlated conductivities controlled by photoirradiation in silver chalcogenolate cluster-based MOFs (SCC-MOFs). We used tetradentate 1,2,4,5-tetracyanobenzene (TCNB) linkers[39] to bridge silver cluster $[Ag_{12}(^{i}PrS)_6]^{6+}$ nodes into a high-dimensional crystalline assembled material[9,40] (**SC-1**). **SC-1** crystals exhibit a complete stoichiometric ratio, approaching perfect single-crystallization (Fig. 1), in which six anionic $[CF_3COO]^-$ and neutral $[CF_3COOH]$ molecules are incorporated in the coordination sphere in addition to guest molecules in the channels of the assembled framework[41]. Upon continuous ultraviolet–visible (UV–Vis) irradiation for five minutes, some of the ligated and free $[CF_3COOH]$ molecules were released, transforming **SC-1** into **SC-2-0.8** and subsequently to **SC-2-0.5** through an in situ single-crystal to single-crystal process[42]. This process resulted in the same space group ($P2_1/c$), in which 0.8/0.5 occupancies of the coordinated $[CF_3COOH]$ molecules and TCNB linkers were found in **SC-2-0.8** and **SC-2-0.5**, at specific positions. **SC-1** was regrown into **SC-3** by lengthening the reaction time. **SC-3** is a vacancy-free single crystal with only one set of three-dimensional (3D) frameworks. Compared with nearly perfect **SC-1** and **SC-3**, the vacancy defects in **SC-2-0.8/0.5** led to the coloring, a broadened UV–Vis absorption spectra, a decreased room-temperature photoluminescence (Supplementary Movie 1), a largely decreased energy

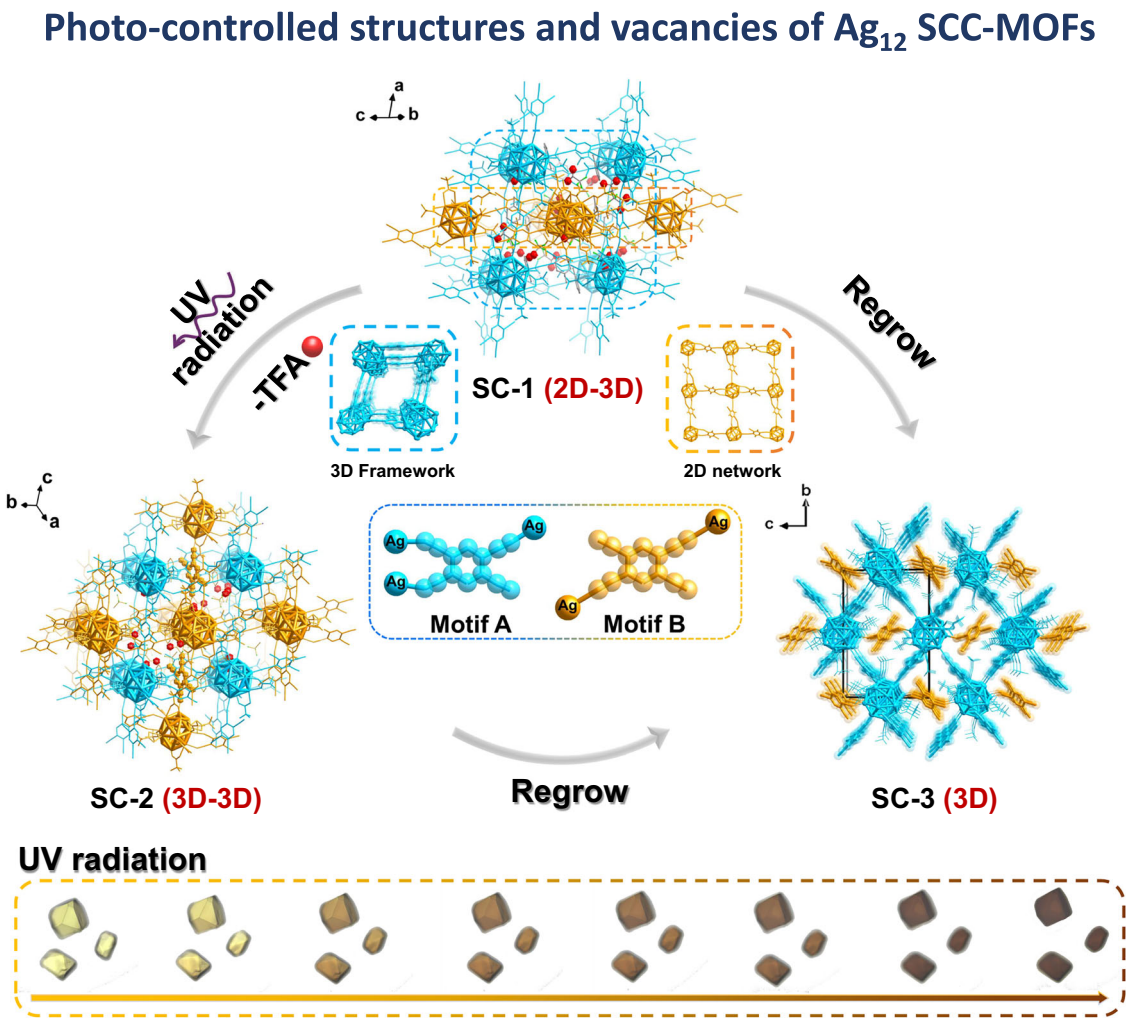

Fig. 1 | Scheme of transformations in SC-1, 2, 3 series. SC-1 Ag_{12} cluster node is bridged by two coordination modes of TCNB ligands (para-coordination, μ_2-η^1 η^1 and 1,2,4-coordination, μ_3-η^1 η^1 η^1). During ultraviolet irradiation, the structure of **SC-1** (2D-3D) is transformed into **SC-2** (3D-3D). The occupancy of the coordinated TFA in **SC-2** is 0.5, and the occupancy of the para-coordinated TCNB is also reduced to 0.5 because of the statistical pattern of the crystal. This course led to a deepened color of single crystals. Furthermore, after being immersed in the mother liquor and kept in a dark environment for over one week, **SC-1** regrows into **SC-3**, which has a 3D non-interpenetrating structure. Color codes: light blue in 3D framework and orange in 2D-network; TFA, red. All hydrogen atoms are omitted for clarity.

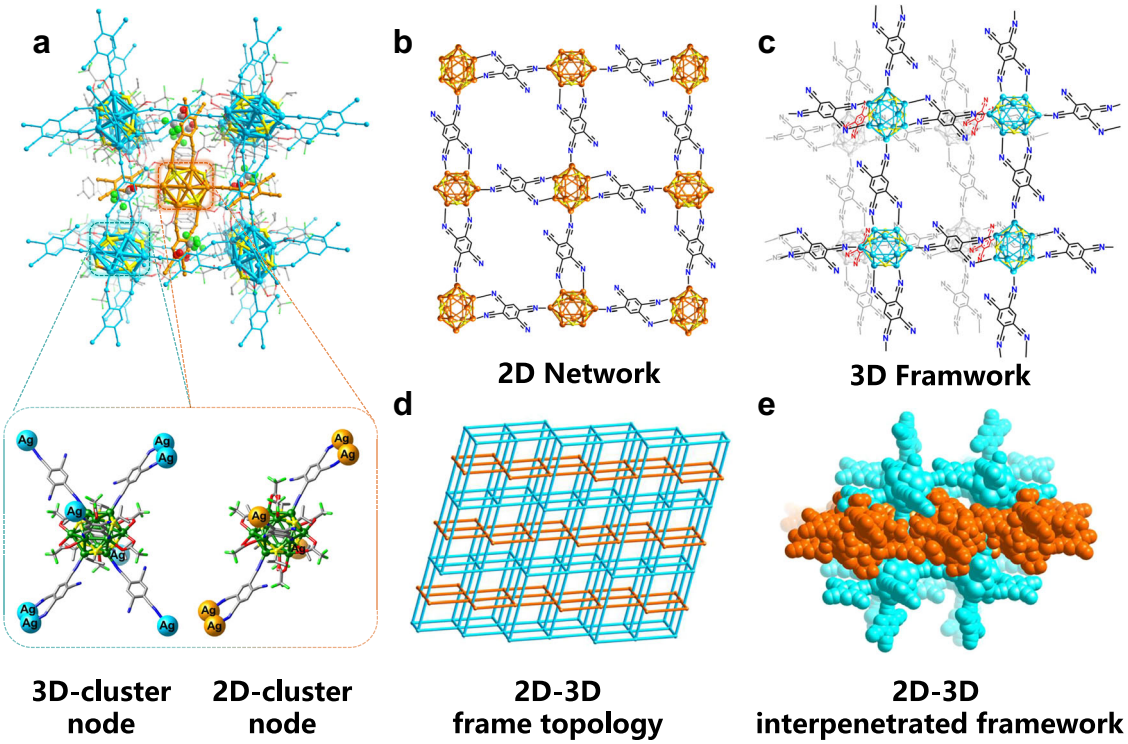

Fig. 2 | The detailed annotation of two-dimensional and three-dimensional interpenetration structure of SC-1. a The frame structure of **SC-1** (the local magnification shows that there are two coordination modes in the interpenetration structure: Ag_{12} cluster is connected to 6 surrounding clusters to form a 3D frame and a Ag_{12} cluster is connected to 4 surrounding clusters to form a 2D network). **b**, **c** the coordination modes of TCNB in two-dimensional network and three-dimensional framework (the gray/shaded structure is located inside the plane to show its three-dimensional character). **d**, **e** 2D-3D frame topology and space-filling mode of **SC-1**. Color code: Ag_{12} cluster, light blue in 3D framework and orange in 2D-network; O, red; F, green C, gray and N, blue, the hydrogen atom is omitted for clarity.

gap, and a 50-fold increased conductivity, which were further confirmed by electron paramagnetic resonance (EPR) and positron annihilation lifetime spectroscopy (PALS), together with single-crystal X-ray diffraction (SCXRD). This method provides a platform for facilitating electronic communication between cluster-building units and creating ordered-vacancy conducting materials.

The formulas of the materials are as follows: **SC-1**, $\{[Ag_{12}(^{i}PrS)_6(CF_3COO)_6(TCNB)_2(CF_3COOH)_2]\cdot[Ag_{12}(^{i}PrS)_6(CF_3COO)_6(TCNB)_3]\}_n$·guests, where guests include $4CF_3COOH$ and $2C_7H_8$ molecules, featuring one set of layer planes interpenetrating another set of 3D frameworks. **SC-2-0.8**, $\{[Ag_{12}(^{i}PrS)_6(CF_3COO)_6(TCNB)_2(TCNB)_{0.5}]\cdot[(CF_3COOH)_{0.8\times2}]\}_{2n}$·guests where guests include $2CF_3COOH$ and $2C_7H_8$ molecules. **SC-2-0.8** is merely obtained as an intermediate state under in situ UV-irradiation and has changed to a two sets of 3D interpenetrating frameworks. **SC-2-0.5** is the resultant stable phase after UV irradiation with a formula of $\{[Ag_{12}(^{i}PrS)_6(CF_3COO)_6(TCNB)_2(TCNB)_{0.5}]\cdot[(CF_3COOH)_{0.5\times2}]\}_{2n}$·guests, where guests include $2CF_3COOH$ and C_7H_8 molecules. **SC-2-0.5** has an interpenetrating framework identical that of **SC-2-0.8**. **SC-2-0.5** features one set of vacancy-free 3D frameworks, with a formula of $\{[Ag_{12}(^{i}PrS)_6(CF_3COO)_6(TCNB)_3]\}_n$·guests, where guests include $2CF_3COOH$ and $2CH_2Cl_2$ molecules.

Results and discussion

Characterization and structural analysis of SC-1, SC-2, and SC-3

The PXRD pattern of three compounds show good crystal purity (Supplementary Fig. 1). Furthermore, the solvent molecules within the framework structure and the extensive hydrogen bonding interactions between TFA, toluene solvent molecules, and bridging ligands enhance the overall stability of the framework. (Supplementary Fig. 2) All the compounds share identical Ag_{12} metal cores but exhibit distinct degrees of distortion and structural framework patterns (Supplementary Figs. 3–5). The two-dimensional (2D) cluster node consists of 12 Ag^+ ions, 6 $^{i}PrS^-$ ions, 8 CF_3COO^- ions, and 4 TCNB bridging ligands. However, the addition of two 1,4-coordinated TCNB ligands to the 3D cluster node, an extension in 3D space is formed (Supplementary Figs. 6 and 7). The twelve silver atoms form a classical cubic octahedron (or truncated cube) skeleton structure composed of eight triangles and six quadrilaterals, resembling one of the thirteen Archimedean polyhedra. The Ag···Ag distance ranges from 2.924(8) Å to 3.278(10) Å. This structure is similar to the Ag_{12} cluster ($[Ag_{12}(^{t}BuS)_6(CF_3COO)_6(CH_3CN)_6]$, **$Ag_{12}$-CN**) reported in a previous work[6]. The sulfur atoms in the six $^{t}BuS^-$ ligands are embedded within the Ag_{12} skeleton through μ_4-η^1 η^1 η^1 η^1 coordination patterns, serving as important templates for forming the six quadrilateral $\{(\mu_4$-$^{t}BuS)\ Ag_4\}$ units with Ag-S bond lengths ranging from: 2.374 Å (8) to 2.684 (17) Å (Supplementary Fig. 8). This can be considered a dodecagonal silver–sulfur cluster core in which the cyano ligands at sites 1 and 4 and at sites 1, 2, and 4 form a 3D expansion in space. (Fig. 2 and Supplementary Fig. 9)

Owing to the coordination of TCNB, the distance between the coordinated silver atoms increases, resulting in local distortion and elongation of the silver skeleton. This structural change is attributed to the electronic and steric effects introduced by TCNB, which further stabilizes the distorted geometry. The previously reported Ag_{12} cluster exhibits similar cyanophenyl coordination with acetonitrile molecules[6]; however, acetonitrile molecules are prone to detachment, making the entire cluster highly unstable. In contrast, the TCNB molecule in **SC-1** remains relatively stable coordinated, leading to relatively improved cluster stability as confirmed by subsequent stability characterization. Topological analysis reveals that **SC-1** possesses a double interpenetration structure with microporosity, contributing to its structural properties. Connecting behavior is observed in which TCNB linkers exhibit two coordination modes. In the 2D layers, three

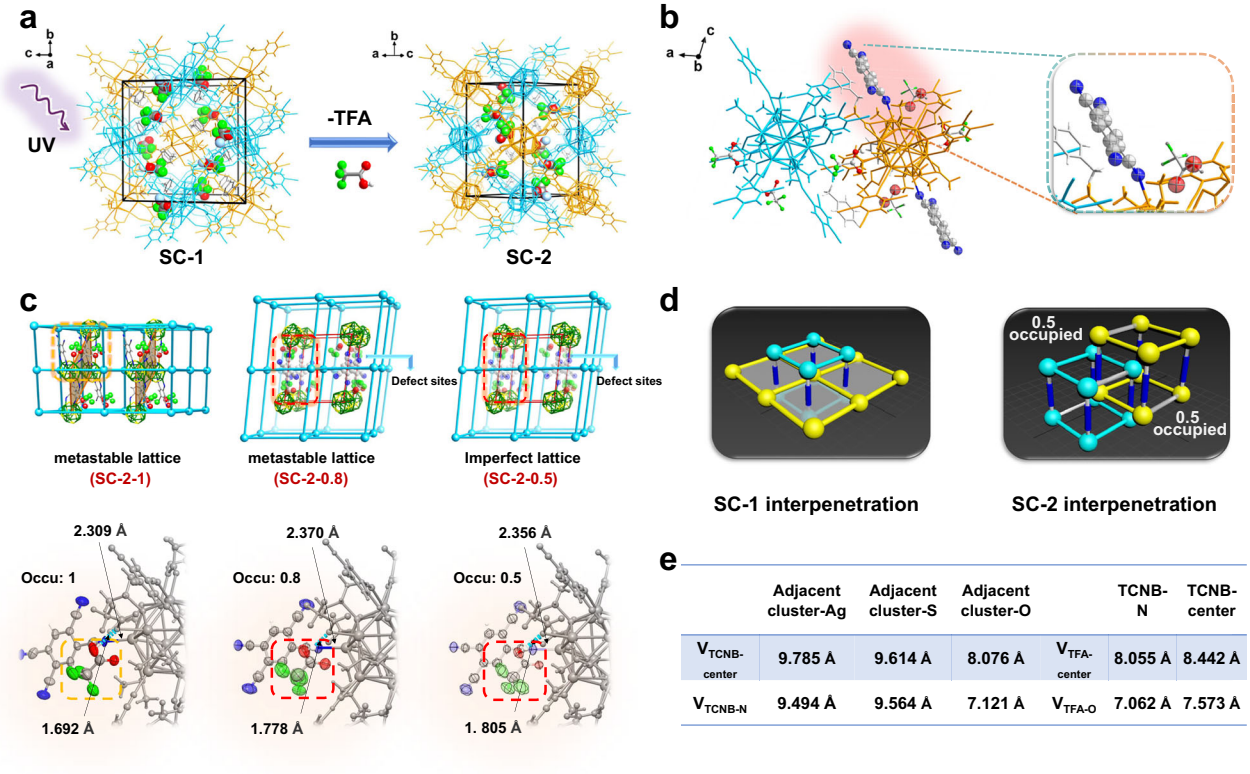

e

	Adjacent cluster-Ag	Adjacent cluster-S	Adjacent cluster-O		TCNB-N	TCNB-center
$V_{TCNB\text{-}center}$	9.785 Å	9.614 Å	8.076 Å	$V_{TFA\text{-}center}$	8.055 Å	8.442 Å
$V_{TCNB\text{-}N}$	9.494 Å	9.564 Å	7.121 Å	$V_{TFA\text{-}O}$	7.062 Å	7.573 Å

Fig. 3 | Schematic illustration of possible mechanisms for the transformations of SC-1 to SC-2. a, **b** Under ultraviolet irradiation, the trifluoroacetic acid molecules overflow from the lattice and the structural symmetry is increased (The para-coordination TCNB occupied 0.5). **c** In situ process from **SC-1** to **SC-2-0.8** and **SC-2-0.5**. Illustration of a stabilization **SC-2-0.5** of UV-induced vacancy defects in SCC-MOFs transformed from metastable **SC-1**; and the detailed annotation of the TCNB coordination modes in 3D-framework and 2D-network in the three compounds. **d** interspersed structures of **SC-1** and **SC-2**. **e** The distance between Ag, S, N atoms of adjacent clusters and the vacancy TCNB and TFA. For clarity, all auxiliary ligands and hydrogen atoms are omitted. Color code: 3D frame cluster node, cyan; 2D network cluster node, gold; 1, 2, 4-coordination TCNB ligand cyan, 1, 4-coordination TCNB ligand, gold; the larger transparent gold atoms represent TCNB ligands that are not fully occupied.

cyano-groups of TCNB participate in μ_3-η^1 η^1 η^1 coordination with Ag–N bond lengths of 2.384 Å, 2.459 Å, and 2.304 Å (Supplementary Fig. 10). Moreover, in the interspersed section of the 3D structure, TCNB exhibits both tri-coordination patterns and a para-cyano coordination mode which enables 3D extension of the 2D layers (Supplementary Fig. 11). In other words, para-cyano groups of TCNB form connections with a Ag–N bond length of 2.384 Å through the μ_2-η^1 η^1 coordination mode. This double interspersed mode generates an almost virtual framework structure with no apertures (Supplementary Fig. 12).

For each 2D Ag_{12} cluster node of **SC-1**, there are only four TCNB ligands anchored to Ag atoms, forming a 2D network structure. The coordination of TCNB and TFA leads to distortion of the Ag_{12} cluster skeleton, resulting in a distance between the upper and lower layers of 5.08 Å. In contrast, the 3D Ag_{12} cluster node of **SC-1** has six TCNB ligands anchored to a Ag atom, creating a 3D extension with relatively symmetric coordination between TCNB and TFA. Consequently, the Ag_{12} cluster node exhibits no distortion and a shortened distance between the upper layer and lower layer of 4.62 Å. The single-crystal structure combined with thermogravimetric analysis (TGA) revealed the presence of toluene molecules in the micropores of **SC-1**. Additionally, three forms of hydrogen bonding interactions were observed in the structure (Supplementary Fig. 2): between uncoordinated TFA and coordinated TFA; TFA acting as a hydrogen bond donor ligand in the μ_1-η^1 form and as a hydrogen bond acceptor ligand in the μ_2-η^1 η^1 form; between toluene solvent molecules and adjacent coordinated TFA. These intermolecular forces further enhance the stability of the framework structure. In contrast to **SC-1, SC-2** crystallizes in the $P2_1/c$ space groups with a double-interpenetrating framework similar to that of **SC-1** (Fig. 2d, e). The bond lengths and angles for each cluster node are detailed in (Supplementary Table 1). Upon transformation from **SC-1** to **SC-2**, it is observed that the Ag-Ag bond lengths of the 2D and 3D cluster nodes in **SC-1** converge towards an average value. Specifically, the Ag-Ag bond lengths in the Ag_{12} cluster of **SC-2** lie between those of the 2D and 3D cluster nodes in **SC-1**.

SC-2 is formed through the transformation of metastable **SC-1** under UV irradiation, resulting in a 3D interpenetrating framework. The structural transformation mechanism we hypothesized is shown in Fig. 3: the loss of TFA leads to vacancy defects, the occupancy of the coordinated TFA in **SC-2** is 0.5, and the occupancy of the para-coordinated TCNB is also reduced to 0.5 because of the statistical pattern of the crystal (Fig. 3a). **SC-3** is also transformed from metastable **SC-1**. As shown in Supplementary Fig. 13, the TCNB ligand is rotated clockwise to adjust its position due to the release of coordinated TFA, resulting in recombination of the framework into a non-interspersed 3D structure within the mother liquor. The Ag12 core is also distorted to a certain extent: the distance between the top Ag_3 unit and the bottom Ag_3 unit is stretched from 4.69 Å to 4.97 Å (Supplementary Fig. 13). TGA; elemental analysis (EA); SCXRD; together with energy-dispersive spectroscopy (EDS) and elemental mapping determined the molecular formula. (Supplementary Figs. 14–16, 20, 21 and Supplementary Tables 8–13).

Transformation from SC-1 to SC-2 via UV irradiation

Single crystals of **SC-2** were obtained by extending the UV irradiation time of **SC-1**. When analyzing the structure, we noted the presence of weakly coordinated trifluoroacetic acid. These molecules can be

https://doi.org/10.1038/s41467-025-60720-6

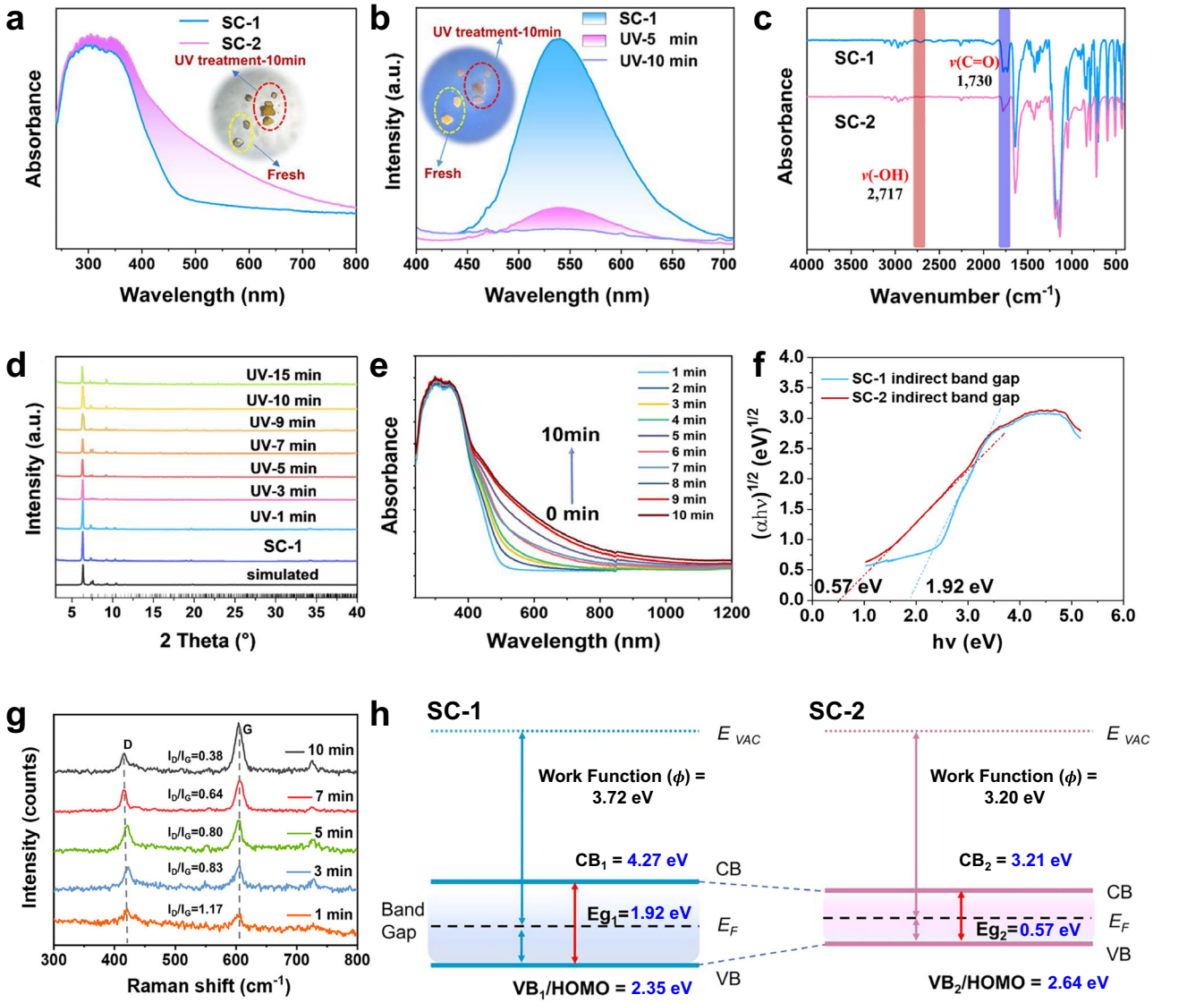

Fig. 4 | Optical properties and energy band structures corresponding to the SC-1 to SC-2 transition process. a Solid-state absorption spectra of **SC-1** crystallites before and after UV treatment (insert: crystallographic contrast of fresh crystals and after UV treatment for 10 min); the pink region represents the change in Solid-state absorption spectrum during the transition from **SC-1** to **SC-2**. **b** Fluorescence spectrum before and after UV treatment for 5 min and 10 min (insert: crystallographic contrast of fresh crystals and after UV treatment for 5 min and 10 min) the blue and pink regions indicate the intensity reduction of fluorescence during 5 min and 10 min, respectively. **c** Infrared spectra of **SC-1** before and after UV treatment for 2 h. **d** PXRD pattern of time-dependent UV treatment. **e** UV-Vis diffuse reflectance spectra of **SC-1** under different UV irradiation times at room temperature. **f** Tauc plot displaying the indirect band gap of **SC-1** and **SC-2**. **g** Raman spectra of pristine and as the UV irradiation time increases, demonstrate that the band structure changes during this process. **h** The valence band, conduction band, and band gap schematic diagram changes before and after UV treatment. VB_1/HOMO = 2.35 eV; VB_2/HOMO = 2.64 eV; Eg_1 = 1.92 eV; Eg_2 = 0.57 eV, and the resulting position of the conduction band are respectively CB_1 = 4.27 eV and CB_2 = 3.21 eV.

removed from the system through ultraviolet irradiation, leading to changes in material properties. An intriguing phenomenon was observed: the color of the single crystal gradually transitioned from transparent light yellow to brown, accompanied by a reduction in the intensity of yellow emission (Fig. 4a, b). The same single crystal was tested in situ after UV irradiation, and was named **SC-2**. The process was monitored through solid absorption and fluorescence spectra analysis. To verify the repeatability and occurrence conditions of this experimental phenomenon, we exposed crystals to UV light under both silicone oil and dry air conditions. Similar changes were observed throughout these processes. (Supplementary Fig. 17) Upon irradiation with UV light, although the solvent and TFA molecules overflow, the interpenetrating framework is still maintained. A detailed comparison (Supplementary Table 2) reveals differences in the bond length and bond angle before and after UV treatment of cluster nodes. Interestingly, while the 2D Ag_{12} cluster node coordinates with 6 TFA ligands, its counterpart in the 3D structure lacks two TFA ligands and connects through 2 TCNB ligands instead. A detailed examination of the single crystal structure revealed that during the structural transformation from one single crystal form to another before and after UV irradiation, solvent molecules together with some TFA molecules originally present within the framework overflowed outwards. This caused significant tensile distortion of the framework structure.

During this UV irradiation transition, more intense long-range π–π stacking and extended C–H···π conjugation occur after desolvation (Supplementary Figs. 18 and 19). Unidirectional stacking facilitates delocalization of electrons over longer distances, thereby enhancing conductivity. This implies that electrons can freely traverse a network of conjugated interactions spanning greater distances. Consequently,

the conductivity of single crystals may be further enhanced. In situ SCXRD combined with TGA reveal that the spillover of TFA and solvent molecules is the important part of the conversion process (Supplementary Fig. 20).

In situ transformation from SC-1 to SC-2 captures the intermediate SC-2-0.8

The in situ SCXRD technique provides a reliable means to analyze atomically precise single crystal structures including the bond length, angle and chemical occupancy. (Fig. 3, Supplementary Tables 2–3) An analysis of each atom and solvent molecule allows understanding how the structure influences the properties. To accurately capture the crystals before and after UV treatment, we selected a high-quality **SC-1-2** single crystal (another good-quality **SC-1** single crystal) for in situ SCXRD analysis. Single crystal diffraction analysis can accurately identify eight coordinated CF_3COO^- ions on 2D nodes and one para-coordinated TCNB ligand used for connection to 3D structures. After the crystal data were collected, UV light was used to irradiate the single crystal in situ for two minutes. An important intermediate **SC-2-0.8** was obtained during the transformation process. The above steps were repeated. After the **SC-2-0.8** data were collected, irradiation was applied again to extend the irradiation time to 10 min, and single-crystal data were collected to obtain diffraction information on **SC-2-0.5** (Fig. 3c). During this process, the color of the single crystal deepens accompanied by a weakening of the yellow fluorescence intensity. We also conducted in situ irradiation experiments on many crystal samples and yield consistent results as for single crystals (Supplementary Tables 10, 11 and 12).

Considering that UV irradiation of crystals generates heat, affecting the transition molecules and TFA overflow, we used two types of light sources (ultraviolet and infrared) to contrast their effects on crystal samples. Control group 1 was exposed to UV light whereas control group 2 was exposed to infrared light simultaneously. The results show that control group 1 exhibits a deeper crystal color and a significantly decreased fluorescence intensity compared to control group 2, indicating that heat has a weaker influence on the transformation of the crystal structure than UV treatment (Supplementary Fig. 21).

Transformation from SC-1 to SC-3 in the mother liquid results in an interpenetration change

After being immersed in the mother liquor and kept in the dark environment for over one week, the crystals were determined to be **Ag_{12}-TCNB 3D (SC-3)**, and the morphology of the single crystals remained largely unchanged, instead forming a non-interpenetrating As depicted in Supplementary Figs. 22 and 23, the comparative analysis of cluster nodes revealed that the coordination bond of TFA and the weak coordination had been disrupted, resulting in a Ag–O bond with a length of 2.7 Å. Due to the dissociation of weakly coordinated TFA, diagonal torsion can be inferred to have occurred within the 1,4-coordination of the cyanide group, which led to a transformation from a double interpenetrating to non-interpenetrating structure for the entire framework; this phenomenon is uncommon during crystal transformation processes.

Characterization and properties of the bridging ligand (TCNB) and the three compounds

The solid luminescence of the ligand TCNB is weak at room temperature and fluorescence cannot be observed by the naked eye under UV irradiation. However, its fluorescence spectrum can be detected via a fluorometer. The optimal emission peak of the TCNB solid ligand occurs at 442 nm. In contrast, in toluene, it appears at 422 nm (Supplementary Fig. 24). The TCNB ligand exhibits a strong diffuse reflection peak in the range of 259–350 nm, which can be attributed to n-π^* transition within the aromatic ligand[43].

Compared to free TCNB ligands, the cluster framework materials formed by TCNB ligands exhibit broader diffuse reflectance edges. In the solid state, **SC-2** shows broader UV-Vis absorption than **SC-1** (Fig. 4a), with the diffuse reflection edges extending from 240 nm to 800 nm. The difference in the absorption peaks before and after UV irradiation can be attributed to solvent and TFA molecule overflow, resulting in different π-conjugated electron pathways. Density functional theory (DFT) calculations reveal that the UV-Vis absorption peak at 350–450 nm is attributed to ligand-to-metal charge transfer (LMCT) from the TCNB ligand to the center of the Ag_{12} silver–sulfur nanoclusters (Supplementary Figs. 25 and 26).

Based on Fourier transform infrared (FT-IR) data, we observed a decrease in the intensities of the peaks at 1730 cm^{-1} and 2717 cm^{-1}, which correspond to the loss of C = O and -OH respectively, from uncoordinated TFA in the framework structure (Fig. 4c)[44–46]. However, PXRD analysis after UV treatment revealed that with increasing UV irradiation time, the XRD peaks at $2\theta = 6.3°$ and 7.3° gradually shift. These peaks correspond to the (0, 1, −1) and (−1, 1, 1) crystal faces and to the (−1, 0, 1) and (0, 0, −2) crystal faces, respectively. The former was obtained by rotating **SC-1** 10° clockwise along the (0, 1, −1) crystal face and 180° vertically along the (0, 1, −1) crystal face. The latter was obtained by rotating **SC-1** by 90° counterclockwise along the (−1, 0, 1) crystal face (Supplementary Figs. 27 and 28). Compared with the simulation results, this finding indicates that powder samples after UV treatment still have good purity in terms of the crystal phase (Fig. 4d).

For **SC-1**, when exposed to 360 nm UV light at room temperature, the sample exhibits yellow fluorescence with an emission peak centered at 540 nm. As depicted in Fig. 4b and Supplementary Figs. 29–31 the optimal excitation wavelength for **SC-1** is 375 nm, whereas the corresponding emission position is 540 nm, a broad emission peak. The DFT calculations indicate that the yellow emission peak observed at 540 nm can be attributed to the metal-to-ligand charge transfer (MLCT) process (Supplementary Figs. 25 and 26). During UV irradiation, fluorescence spectroscopy measurements revealed a pronounced decrease in fluorescence intensity. Compared with the yellow emission of **SC-1**, the crystal sample exhibits a significantly weakened photoluminescence (PL) intensity after UV treatment. The band gap was calculated via the Vienna Ab initio Simulation Package (VASP) in conjunction with the partial density of states (PDOS), indicating an indirect band gap for the three compounds. The Tauc diagrams of the optical band gaps at the beginning and end of the transition process were estimated to be 1.92 eV and 0.57 eV (experimental value), respectively (Figs. 4e, f and Supplementary Figs. 32–35).

The TGA curves demonstrate a sequential loss of solvent molecules (TFA and toluene) from the framework structure during the heating process (Supplementary Fig. 20). This gradual solvent evaporation can also be observed through SCXRD. In other words, the overflow of solvent molecules increases the symmetry of the skeletal structure and changes in the bond lengths. The gravimetric isothermal adsorption curves and adsorption capacity-time curves of the three compounds are shown in Supplementary Figs. 36–38. By comparing the cluster nodes and charge density diagrams of **SC-1** ~ **3**, we can conclude that the occupancy of TFA molecules decreases from the full occupancy for **SC-1** to a 0.5 occupancy for **SC-2**, with stretching of the Ag–O bond length (2.374 (4) Å to 2.450 (5) Å) and the Ag–N bond length (2.322 (2) Å to 2.478 (4) Å) (Supplementary Figs. 39, 40).

The energy levels of **SC-1** and **SC-2** were determined through ultraviolet photoelectron spectroscopy (UPS) analysis, where tangents were drawn to the band edges in the UPS spectra (Supplementary Fig. 41). The intersection points with the lower end indicate the location of the valence band and the work function. Based on this analysis, after UV treatment, there is a shift in the valence band from 2.35 eV to 2.64 eV and correspondingly a change in the work function from 3.72 eV to 3.20 eV during the process (Supplementary Fig. 41a–f). After UV treatment, electrons in the valence band are more likely to transition to the conduction band because of the narrower band gap (Fig. 4h).

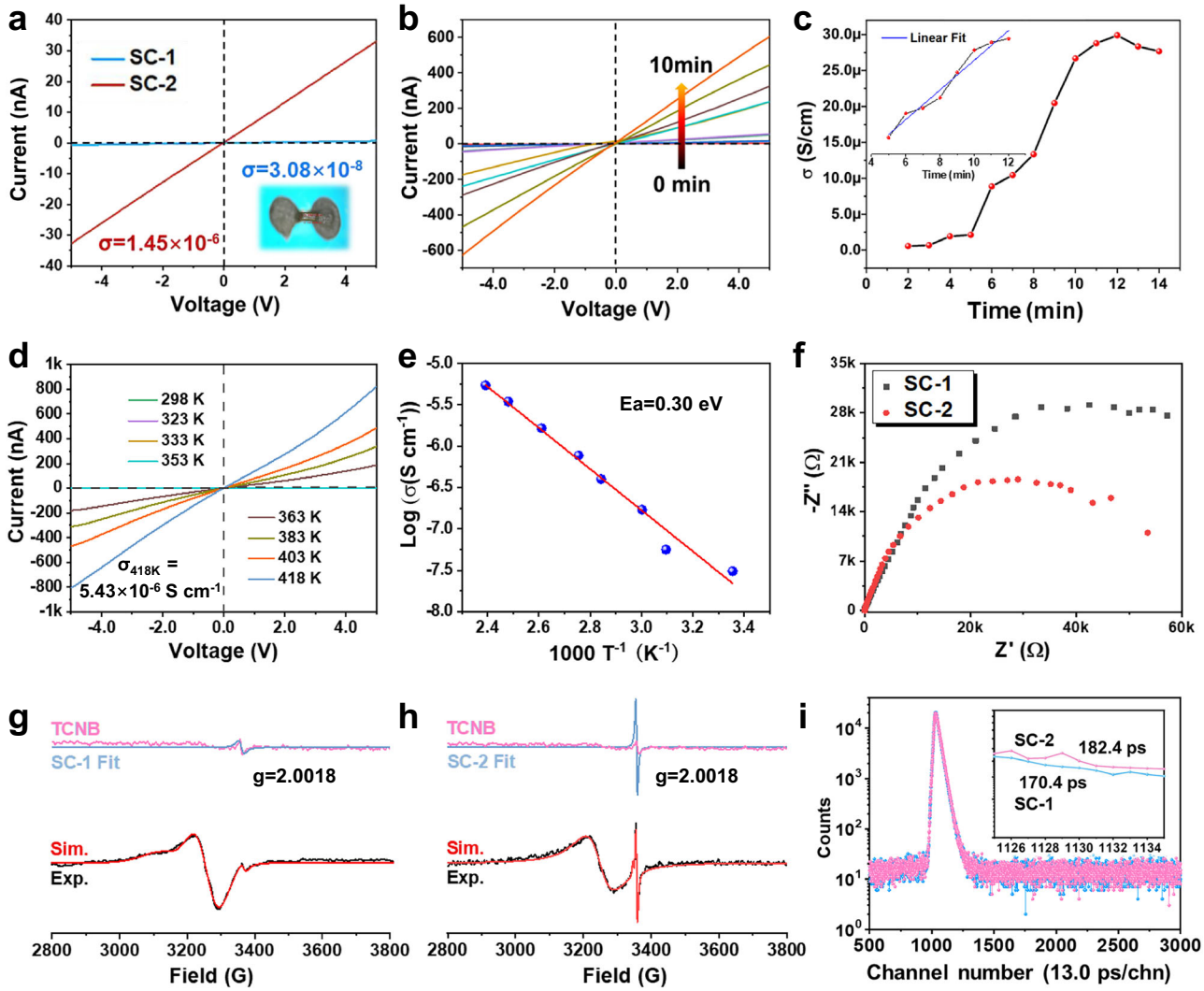

Fig. 5 | Electrical properties and defect characterization of SC-1 and SC-2. a The I-V curves of **SC-1** and **SC-2** (insert: single crystal I-V curve test device illustration, silver paste at both ends of the crystal). **b** Time-dependent I-V curves under UV treatment. **c** Time-dependent electrical conductivity under UV treatment from 2 to 14 min (insert: The conductivity of UV treatment showed a similar linear increase for 5–12 min). **d** temperature-dependent I–V curves of **SC-1**, variable temperature I-V curves of 298 K-353 K were depicted in Supplementary Fig. 42. **e** Arrhenius linear fitting of temperature change. **f** Electrochemical Impedance Spectroscopy of **SC-1, 2**. **g**, **h** EPR spectrum (black curve) and EPR simulation result (red curve) of **SC-1, SC-2** and TCNB (pink line) at 2 K. Normalized ultralow temperature 2 K blue line weak signal at $g = 2.0018$. **i** PALS spectra of **SC-1** and **SC-2**.

Electrical conductivity of single crystals during the transformation

Compared with the free ligands, the SCC-MOFs formed from the TCNB ligands present broader diffuse reflection peaks (Fig. 4e and Supplementary Fig. 24). Upon exposure to UV irradiation or heat treatment, the solid-state UV–Vis absorption spectrum of **SC-1** shows a significant extension of the absorption band. This extension is attributed to the expansion of the π–π conjugated system after the TFA loss, forming a new conjugated π electronic pathway.

Due to the narrowing of the optical band gap, there may be a significant difference between the conduction band and valence band phases, impacting the conductivity. The I–V curves were measured via the double probe contact method before and after the transformation (Fig. 5a, and Supplementary Fig. 43). The conductivity after UV treatment is nearly fifty times greater (Fig. 5b). Specifically, at room temperature, the conductivity reaches 1.45×10^{-6} S cm^{-1} which is significantly higher than the value of untreated crystal samples of 3.08×10^{-8} S cm^{-1} (Fig. 5a). The I–V curves demonstrate that the conductivity is directly proportional to the treatment time during this process with an almost linear increase over a period of five to twelve minutes (Fig. 5c). Temperature-dependent conductivity tests revealed an increase in the conductivity up to 5.43×10^{-6} S cm^{-1} at 418 K (Fig. 5d). The plot illustrating the conductivity against temperature exhibits a linear Arrhenius-type dependence (Fig. 5e). The narrowing of the band gap and increase in the conductivity with increasing temperature indicate the semiconductor properties of **SC-2**. The electrical conductivity of **SC-3** is consistent with that of **SC-1** (Supplementary Figs. 43 and 44).

EPR studies were then conducted to further determine the vacancy defect state of the Ag_{12}-TCNB series (Fig. 5g, h) (i.e., Exp. Data in Supplementary Tables 3 and 4). A relatively weak but sharp resonance signal is centered at 3359 T ($g = 2.0018$), indicating the intrinsic EPR signal of the TCNB ligand. The EPR signal of the **SC-1** crystal was fitted to two signals. The larger symmetric broad peak indicating spin magnetic behavior could originate from the unpassivated dangling bonds of surface atoms[47], and a weak peak corresponding to the TCNB intrinsic EPR signal still appeared. For **SC-2**, except for the peaks of Ag clusters, the fitted g value is also centered at 2.0018. It is significantly enhanced, consistent with the process of vacancy defect generation by irradiation, so we attribute it to the peak of the intrinsic EPR signal of

the TCNB ligand, TCNB vacancies and TFA vacancies. In contrast, the EPR spectrum of **SC-3** is similar to that of **SC-1** in that only a weak signal of TCNB appears (Supplementary Fig. 45). The changes in the **SC-1** and **SC-2** EPR signals, demonstrating an increase in the defect density during the UV irradiation process.

PALS is a well-established technique that characterizes the vacancies and defects in materials. Three lifetimes were fitted for both **SC-1**(τ_1 = 170.4 ps, τ_2 = 368.7 ps, τ_3 = 1.12 ns) and **SC-2** (τ_1 = 182.4 ps τ_2 = 378.3 ps τ_3 = 1.21 ns). The PALS spectra before and after UV irradiation are shown in Fig. 4i. τ_1 is assigned to lattice defects, including structural vacancies (τv), whereas τ_2 is caused by vacancy clusters[48]. Specifically, after UV irradiation, the relaxation time of the lattice defects τ_1 and the relaxation time of the vacancy defects τ_2 are significantly extended (Table S5) which suggests that more vacancy defects are introduced, consistent with the EPR results. This also indicates that UV irradiation stabilizes of these defects—either by increasing the number of such defects or by altering their energetic state so that they become less mobile or more difficult to annihilate. (Fig. 4i). The Ag 3 d XPS spectra together with auger peaks, reveal the presence of Ag^0 in the blue region of **SC-2** (Supplementary Figs. 46–47) which further shows that some surface silver ions can be reduced by UV irradiation to promote the generation of defect states. The in situ XPS O 1s spectra for **SC-1** during UV irradiation also indicate the formation of vacancy defects (Supplementary Fig. 48).

Bonding length analysis and DFT calculations on the interaction energy of the coordination CF_3COOH provide insight into the intrinsic mechanism of the transformation. The bond length of the CF_3COOH Ag-O bond forming a vacancy defect in **SC-1** is more significant than that of CF_3COO^-—at other coordination sides of **SC-1**. This implies that the bond energy of the Ag-O bond in this study is lower than these values. We calculated the interaction energy of the coordination CF_3COOH in the periodic structure through two optimization calculation models, and the resulting data were 166.356 kJ mol^{-1} and 167.999 kJ mol^{-1}, respectively, which are nearly identical (including surrounding interaction forces such as hydrogen bonds) (Supplementary Tables 14 and 15). For typical Ag-O coordination bonds, the bond energy is reported to be 220.1 ± 20.9 kJ mol^{-1} [49]. Since this value exceeds the interaction energy of those trifluoroacetic acid weakly ligated silver clusters, it elucidates why UV irradiation 'selectively' disrupts the weakly coordinated trifluoroacetic acid in this scenario. Upon removal of TFA under ultraviolet irradiation, the angles of the TCNB ligands are altered, thereby inducing adaptive changes in the entire framework structure. Thus, a synergistic effect promoted the structure transformation and consequently enhanced conductivity.

In summary, this study demonstrates the potential of using vacancy engineering to improve electronic communication between cluster units in 3D orientationally ordered SCC-MOF crystals. This advancement resulted in an increase in the single-crystal conductivity, with improvements of up to 50-fold. The chemical flexibility and structural rigidity of SCC-MOFs enable a sensitive photo-response of weak coordination bonds while preserving the framework structure in a single-crystal state. We employed in situ SCXRD analysis, along with EPR, PALS, band-gap analysis, and electron density analysis, to investigate the irradiation-time dependence of the conductivity. This comprehensive approach establishes a clear connection between the structure, vacancies, and conductivity of SCC-MOFs. This innovative strategy opens avenues for developing cluster assemblies in crystalline optoelectronic materials, advancing the exploration of disordered crystalline materials with ordered structures.

Methods

Synthesis of isopropyl silver sulfide (^{i}PrSAg)

Use an analytical balance to weigh $AgNO_3$ (5 g, 0.03 mol) and add it into 170 mL of acetonitrile solution, stir and dissolve to obtain a colorless transparent solution. Add 2.8 mL 2-Propanethiol and 5 mL triethylamine to the solution, and immediately obtain a yellow suspension solution. Continue to stir away from light for 3 h, and then filter. Washed with 10 mL ethanol and 20 mL ether, the light-yellow solid obtained by drying at room temperature is the product. (92% yield, based on $AgNO_3$).

Synthesis of silver trifluoroacetic acid (CF_3COOAg)

Ag_2O (12 g, 0.05 mol) was added to 100 mL of water and stirred to obtain a black mixed solution. and continuously stir it to obtain a black mixed solution. Add 8 mL of CF_3COOH to it until the precipitate is completely dissolved, and then continue stirring in the dark for 10 h to obtain a colorless and transparent solution. Then filter to remove impurities, transfer the colorless filtrate to a 250 mL Round-bottom flask, and add acetonitrile to spin dry the white precipitate obtained as the product. (Yield is 85.2% based on Ag).

Ag_{12}-TCNB series were synthesized through a facile 'one-pot' method. In brief, TCNB was added to the mixed solvent system of DCM, toluene containing CF_3COOAg, $\{^i PrSAg\}_n$ and CF_3COOH (TFA), forming a yellow clear solution. Yellow block crystals were collected after evaporation of solvents under ambient conditions for 3 days. In the synthetic process, the suitable binary solvent system is crucial for the formation of **Ag_{12}** and crystal growth. The lack or changing of some solvents, even the adjustment of toluene dosage cannot effectively synthesize the crystalline product. The crystals were initially filtered under intense agitation, but this process produces powder crystals and the crystal yield is low. Later adjust the conditions and stir slightly with a glass rod before the powder crystal has produced, direct filtration to increase the yield.

Synthesis of single crystal SC-1

^{i}PrSAg (15 mg, 0.03 mmol) was dispersed in a mixed solution of 2 mL toluene and 4 mL dichloromethane to obtain a faint yellow emulsion, to which TCNB (8 mg, 0.045 mmol) was added. After stirring vigorously for 5 min, absorb 15 μL CF_3COOH and add it, weigh CF_3COOAg (20 mg, 0.1 mmol) and add it to the above solution, stir thoroughly and filter. Put the filtrate in a dark place to avoid light and volatilize for about 2 days to get yellow massive crystals, wash the crystals with methylene chloride and collect them. (Yield 42.7%, based on Ag).

The transformation from SC-1 to SC-2

SC-2 is transformed from metastable **SC-1** by ultraviolet irradiation, resulting in a three-dimensional interpenetrating framework. Upon continuous ultraviolet–visible (UV–Vis) irradiation for five minutes, some of the ligated and free [CF_3COOH] molecules escaped, transforming **SC-1** into **SC-2** through an in situ single-crystal to single-crystal process.

The transformation from SC-1 to SC-3

The TCNB ligand is rotated clockwise to replace its position due to the shedding of the coordination trifluoroacetic acid, resulting in the recombination of the frame into a non-interspersed three-dimensional structure in the mother liquor. Immerse in the mother liquor and store in the dark for more than a week to obtain **SC-3** single crystal. It was observed that the single crystal morphology remained essentially unchanged but formed a non-interpenetrating structure (Supplementary Fig. 13).

Electrical measurement and fabrication of single crystal electrode

The electric conductivity measurement was realized by a semiconductor analyzer (B1500A, Keysight), and the electrode device is in a probe station (CGO-4, Cindbest) with HT-400 Thermostat. The single-crystal electrodes were made using SPI conductive silver paint (SPI 05002-AB) by placing the crystal between two electrodes. The sizes of

the crystals are measured by a RX50M metalloscope. After conducting multiple tests, we have determined the range of conductivity variation during the transformation process and have observed a consistent pattern: there is a certain degree of reduction in contact resistance as the selected single crystal is smaller and thinner. (When the prepared device is placed in the air atmosphere for a period of time and then tested, the conductivity will be reduced to a certain extent, but the trend of increasing conductivity remains almost consistent with the increase of UV irradiation time).

Preparation of single crystal conductivity measuring device

In brief, the **Ag_{12}-TCNB 2D-3D (SC-1), Ag_{12}-TCNB 2D-3D UV (SC-2) and Ag_{12}-TCNB 3D (SC-3)** crystals were individually placed onto Si/SiO_2 substrates using a crystal picking needle, and silver paste was dropped on both ends of the crystals for device construction. After drying in air for 12 h, the two segments of the silver paste were contacted with a gold probe to establish electrical contact between the crystal and the electrode. Positive and negative poles were connected to the device respectively for conductivity measurement. All electrical measurements were conducted at room temperature under dark conditions. More than 5 devices were examined in this study, demonstrating nearly identical electrical conductivity and temperature-dependent behavior. Current-voltage (I–V) curves of single crystal devices were collected using a semiconductor analyzer (Keysight B1500A). The electrical conductivity was determined from the slope of the linear I–V curves. The diameter and length of each crystal were measured using an optical microscope with length being measured from edge to edge of the contacts. Blank samples without crystals were also tested; however, only the noise background was observed indicating that conductivity is solely contributed by the crystals themselves.

Data availability

All data are available from the corresponding author upon request. The data generated in this study are provided in the Supplementary Information/Source Data file. The X-ray crystallographic coordinates for structures reported in this study have been deposited at the Cambridge Crystallographic Data Centre (CCDC), under deposition numbers CCDC 2384559 (**SC-1**), 2384560 (**SC-2**), 2384561 (**SC-3**), 2384562 (**SC-2-1**), 2384563 (**SC-2-0.8**) and 2384564 (**SC-2-0.5**). These data can be obtained free of charge from The Cambridge Crystallographic Data Centre via www.ccdc.cam.ac.uk/data_request/cif. Source data are provided with this paper.

References

1. Doud, E. A. et al. Superatoms in materials science. *Nat. Rev. Mater.* **5**, 371–387 (2020).
2. Chang, H. et al. Highly fluorescent gold cluster assembly. *J. Am. Chem. Soc.* **143**, 326–334 (2021).
3. Liu, Q. & Wang, X. Fabricating sub-nanometer materials through cluster assembly. *Chem. Sci.* **13**, 12280–12289 (2022).
4. Zhang, F., Li, H., Li, Z., Liu, Q. & Wang, X. Phase engineering of polyoxometalate assembled superstructures. *Nat. Synth.* **3**, 1039–1048 (2024).
5. Jin, R., Zeng, C., Zhou, M. & Chen, Y. Atomically precise colloidal metal nanoclusters and nanoparticles: fundamentals and opportunities. *Chem. Rev.* **116**, 10346–10413 (2016).
6. Huang, R.-W. et al. Hypersensitive dual-function luminescence switching of a silver-chalcogenolate cluster-based metal–organic framework. *Nat. Chem.* **9**, 689–697 (2017).
7. Dong, X.-Y. et al. Ligand engineering to achieve enhanced ratiometric oxygen sensing in a silver cluster-based metal-organic framework. *Nat. Commun.* **11**, 3678 (2020).
8. Wang, J.-Y. et al. Engineering intelligent chiral silver cluster-assembled materials for temperature-triggered dynamic circularly polarized luminescence. *Aggregate* **5**, e508 (2024).
9. Vogel, N., Retsch, M., Fustin, C.-A., del Campo, A. & Jonas, U. Advances in colloidal assembly: the design of structure and hierarchy in two and three dimensions. *Chem. Rev.* **115**, 6265–6311 (2015).
10. Jin, Y., Zhang, C., Dong, X.-Y., Zang, S.-Q. & Mak, T. C. W. Shell engineering to achieve modification and assembly of atomically-precise silver clusters. *Chem. Soc. Rev.* **50**, 2297–2319 (2021).
11. Kurashige, W., Niihori, Y., Sharma, S. & Negishi, Y. Precise synthesis, functionalization and application of thiolate-protected gold clusters. *Coord. Chem. Rev.* **320-321**, 238–250 (2016).
12. Matus, M. F. & Häkkinen, H. Understanding ligand-protected noble metal nanoclusters at work. *Nat. Rev. Mater.* **8**, 372–389 (2023).
13. Li, Y. et al. Self-assembly of chiroptical ionic co-crystals from silver nanoclusters and organic macrocycles. *Nat. Chem.* **17**, 169–176 (2025).
14. Schubert, U. Cluster-based inorganic–organic hybrid materials. *Chem. Soc. Rev.* **40**, 575–582 (2011).
15. Ong, W.-L. et al. Orientational order controls crystalline and amorphous thermal transport in superatomic crystals. *Nat. Mater.* **16**, 83–88 (2017).
16. Buonsanti, R. Magic clusters are better together. *Nat. Mater.* **20**, 580–581 (2021).
17. Yang, J. et al. Superatomic solid solutions. *Nat. Chem.* **13**, 607–613 (2021).
18. Li, Q. et al. Modulating the hierarchica fibrous assembly of Au nanoparticles with atomic precision. *Nat. Commun.* **9**, 3871 (2018).
19. Yuan, P. et al. Solvent-mediated assembly of atom-precise gold–silver nanoclusters to semiconducting one-dimensional materials. *Nat. Commun.* **11**, 2229 (2020).
20. Bootharaju, M. S. et al. Structure of a subnanometer-sized semiconductor Cd14Se13 cluster. *Chem* **8**, 2978–2989 (2022).
21. Zeng, C., Chen, Y., Kirschbaum, K., Lambright, K. J. & Jin, R. Emergence of hierarchical structural complexities in nanoparticles and their assembly. *Science* **354**, 1580–1584 (2016).
22. Cook, A. W. & Hayton, T. W. Case studies in nanocluster synthesis and characterization: challenges and opportunities. *Acc. Chem. Res.* **51**, 2456–2464 (2018).
23. Fan, K. et al. Single crystals of a highly conductive three-dimensional conjugated coordination polymer. *J. Am. Chem. Soc.* **145**, 12682–12690 (2023).
24. Das, A. K. et al. Two-dimensional silver-chalcogenolate-based cluster-assembled material: a p-type Semiconductor. *Nano Lett.* **23**, 8923–8931 (2023).
25. Liu, K.-G. et al. A conductive 1D high-nucleus silver polymer as a brilliant non-hybrid supercapacitor electrode. *J. Mater. Chem. A* **8**, 12975–12983 (2020).
26. Zhang, J., Feng, P., Bu, X. & Wu, T. Atomically precise metal chalcogenide supertetrahedral clusters: frameworks to molecules, and structure to function. *Natl. Sci. Rev.* **9**, nwab076 (2022).
27. Chong, S., Rogge, S. M. J. & Kim, J. Tunable electrical conductivity of flexible metal–organic frameworks. *Chem. Mater.* **34**, 254–265 (2022).
28. Simonov, A. & Goodwin, A. L. Designing disorder into crystalline materials. *Nat. Rev. Chem.* **4**, 657–673 (2020).
29. Gu, Z.-X. et al. Molecular orbital breaking in photo-mediated organosilicon Schiff base ferroelectric crystals. *Nat. Commun.* **15**, 4416 (2024).
30. Jorgensen, J. D. et al. Structural properties of oxygen-deficient $YBa_2Cu_3O_7$–δ. *Phys. Rev. B* **41**, 1863–1877 (1990).
31. Simonov, A. et al. Hidden diversity of vacancy networks in Prussian blue analogues. *Nature* **578**, 256–260 (2020).
32. Boström, H. L. B., Bruckmoser, J. & Goodwin, A. L. Ordered B-Site vacancies in an ABX3 Formate Perovskite. *J. Am. Chem. Soc.* **141**, 17978–17982 (2019).
33. Bennett, T. D., Cheetham, A. K., Fuchs, A. H. & Coudert, F.-X. Interplay between defects, disorder and flexibility in metal-organic frameworks. *Nat. Chem.* **9**, 11–16 (2017).

34. Fang, Z., Bueken, B., DeVos, D. E. & Fischer, R. A. Defect-engineered metal–organic frameworks. *Angew. Chem. Int. Ed.* **54**, 7234–7254 (2015).
35. Razumovskiy, V. I., Ruban, A. V., Odqvist, J. & Korzhavyi, P. A. Vacancy-cluster mechanism of metal-atom diffusion in sub-stoichiometric carbides. *Phys. Rev. B* **87**, 054203 (2013).
36. Benavides, K. A., Oswald, I. W. H. & Chan, J. Y. Casting a wider net: rational synthesis design of low-dimensional bulk materials. *Acc. Chem. Res.* **51**, 12–20 (2018).
37. Li, S., Li, N.-N., Dong, X.-Y., Zang, S.-Q. & Mak, T. C. W. Chemical flexibility of atomically precise metal clusters. *Chem. Rev.* **124**, 7262–7378 (2024).
38. Schmidbaur, H. & Schier, A. Argentophilic interactions. *Angew. Chem. Int. Ed.* **54**, 746–784 (2015).
39. Iwata, S., Tanaka, J. & Nagakura, S. Molecular complexes between 1,2,4,5-Tetracyanobenzene and some aromatic electron donors. *J. Am. Chem. Soc.* **88**, 894–902 (1966).
40. Gong, C.-H. et al. Epitaxial coordination assembly of a semi-conductive silver-chalcogenide layer-based MOF. *Chem. Commun.* **58**, 1788–1791 (2022).
41. Lo, S.-H. et al. Rapid desolvation-triggered domino lattice rearrangement in a metal–organic framework. *Nat. Chem.* **12**, 90–97 (2020).
42. Wang, W. et al. Ultrafast single-crystal-to-single-crystal transformation from metal–organic framework to 2D hydroxide. *Adv. Mater.* **34**, 2106400 (2022).
43. He, B. et al. Clusteroluminescence from cluster excitons in small heterocyclics free of aromatic rings. *Adv. Sci.* **8**, 2004299 (2021).
44. Tian, Y.-Q. et al. Atomically accurate site-specific ligand tailoring of highly acid- and alkali-resistant Ti(iv)-based metallamacrocycle for enhanced CO_2 photoreduction. *Chem. Sci.* **14**, 14280–14289 (2023).
45. Campbell, B. M. et al. Electrophotocatalytic perfluoroalkylation by LMCT excitation of Ag(II) perfluoroalkyl carboxylates. *Science* **383**, 279–284 (2024).
46. Bai, R. et al. Strong electron-withdrawing effect activates metal-free carboxylate anion into efficient active sites for electrocatalytic acetylene semihydrogenation. *J. Am. Chem. Soc.* **147**, 6880–6885 (2025).
47. Ma, M.-X. et al. A nanocluster $[Ag_{307}Cl_{62}(SPhtBu)_{110}]$: chloride intercalation, specific electronic state, and superstability. *J. Am. Chem. Soc.* **143**, 13731–13737 (2021).
48. Luo, Z. et al. Chemically activating MoS_2 via spontaneous atomic palladium interfacial doping towards efficient hydrogen evolution. *Nat. Commun.* **9**, 2120 (2018).
49. Christian, J. D. Strength of chemical bonds. *J. Chem. Educ.* **50**, 176 (1973).

Acknowledgements

This work was supported by the National Natural Science Foundation of China (No. 92461304, S.Q.Z.; U21A20277, X.Y.D.; 22171248, H.Y.L.), the Zhongyuan Thousand Talents (Zhongyuan Scholars) Program of Henan Province (No. 234000510007, S.Q.Z.), the Excellent Youth Foundation of Henan Scientific Committee (232300421022, X.Y.D.), and Zhengzhou University. the Program for Innovative Research Team (in Science and Technology) in University of Henan Province, (IRTSTHN, 25IRTSTHN001, X.Y.D.).

Author contributions

S.Q.Z. and H.Y.L. conceived and designed the experiments. K.M. and X.M.L. (Xue-Mei Liu) conducted the synthesis and characterization. K.M. and X.M.L. (Xi-Ming Luo) drew pictures in the manuscript. K.M., X.Y.D., X.M.L. (Xi-Ming Luo), and H.Y.L. analyzed the experimental results. K.M. completed the original draft writing. X.Y.D., H.Y.L., S.Q.Z., and Thomas C. W. Mak reviewed and edited the manuscript.

Competing interests

The other authors declare no competing interests.

Additional information

Supplementary information The online version contains supplementary material available at https://doi.org/10.1038/s41467-025-60720-6.

Correspondence and requests for materials should be addressed to Hai-Yang Li or Shuang-Quan Zang.

Peer review information *Nature Communications* thanks Junkuo Gao, and the other, anonymous, reviewer(s) for their contribution to the peer review of this work. A peer review file is available.